Supporting Information

# Manipulating ligand effects over Pt-Ni solid-solution alloys for highly efficient ammonia electrooxidation

*Weiyi Shen,‡ Qingyi Yan,‡ Lifang Zhang,* Huiru Sang, Sisi Liu, Xiaolei Yuan, Wenjun Shi, Yutong Zhu, Xinyu Ding,* and Tao Qian**

School of Chemistry and Chemical Engineering, Nantong Key Laboratory of Green Hydrogen-Ammonia Energy Storage and Conversion, Nantong University, Nantong 226019, China.

*Corresponding authors: lfzhang@ntu.edu.cn (L. Zhang); ding.xyu@ntu.edu.cn (X. Ding); qiantao@ntu.edu.cn (T. Qian)

‡ These authors contributed equally.

**Experimental section**

**Synthesis of A-$Pt_xNi_y$@NPC.** 1.5 g of sodium alginate was dissolved in 100 mL of deionized water, resulting in a 1.5 wt.% solution. A mixture of 0.1 M platinum nitrate ($Pt(NO_3)_2$) and 0.1 M nickel nitrate ($Ni(NO_3)_2 \cdot 6H_2O$) aqueous solution was added. After stirring for 24 h, the mixture was transferred to an autoclave and heated at 140 ℃ for 8 h. The resulting product was finally vacuum-dried and grounded. The obtained powders were placed in a tubular furnace and carbonized at 700 °C for 1 h under a nitrogen atmosphere, with a heating rate of 5 ℃ $min^{-1}$. After natural cooling to room temperature, the A-$Pt_7Ni_1$@NPC was obtained. A-$Pt_{10}Ni_1$@NPC, A-$Pt_5Ni_1$@NPC, and A-Pt@NPC were synthesized using the same synthesis method with the only change of the amounts of $Pt(NO_3)_2$ and $Ni(NO_3)_2 \cdot 6H_2O$.

**Physical characterization.** Measurements of the catalyst composition was performed using inductively coupled plasma optical emission spectrometry (ICP-OES, Optima 8000). The morphologies of the samples were examined using a field emission SEM (SU8010, Japan) and a field emission transmission electron microscope (FEI Tecnai G2 F20 S-TWIN TMP, Hong Kong). The aberration-corrected high-angle annular dark-field scanning transmission electron microscopy (AC HAADF-STEM) images and energy dispersive X-ray spectroscopy (EDS) maps were taken on a JEOL ARM 200F scanning transmission electron microscope. An ASAP 2020 accelerated surface area and porosimetry instrument (Micromeritics) was used to conduct $N_2$-physisorption analysis. The physical structure of samples was characterized by an X-ray diffraction (D8 Advance, Bruker) and Raman spectroscopy (HR evolution, Horiba Jobin Yvon). Surface elemental analysis was performed using X-ray photoelectron spectroscopy (XPS, Escalab 250Xi).

**Preparation of working electrode.** A rotating disk electrode (RDE) with a glassy carbon (GC, diameter: 5.0 mm) covered by a catalyst film acts as a working electrode. The catalyst ink was prepared by ultrasonicating a mixture of 2 mg catalyst, 0.5 mg carbon black, 40 μL of 5 wt.% Nafion solution, and 460 μL ethanol to form a homogeneous dispersion. Following the drop-casting of 25 μL catalyst ink onto the RDE center, the electrode was dried at room temperature to yield a uniform catalytic film. The total mass of the catalyst loaded on the GC electrode is precisely 0.1 mg. To

provide a fair and practical evaluation of the intrinsic catalytic performance, the mass activities of all synthesized samples and the commercial PtIr/C reference were strictly normalized based on the precise mass of Pt loaded on the working electrode, which was determined by ICP-OES measurements.

**Electrochemical measurements.** Electrochemical measurements were conducted using a RDE (PINE, AFMSRCE) coupled with a WaveDriver 20 bipotentiostat (Pine Instrument Company, USA). The counter electrode was a platinum (Pt) wire, and the reference electrode was an Ag/AgCl (4 M KCl) electrode. All potentials without specifying were converted to the reversible hydrogen electrode (RHE) using the following equation:

$$E\ (RHE) = E\ (Ag/AgCl) + 0.0591 \times pH + 0.196\ V \quad (1)$$

The catalyst-coated disk working electrode was initially activated by CV from 0.223 to 1.123 V versus RHE in 1.0 M KOH solution at a scan rate of 100 mV $s^{-1}$ until a stable CV curve was obtained. Subsequently, CV curves were recorded at a scan rate of 5 mV $s^{-1}$ while maintaining a rotation rate of 900 rpm. Then, the AOR activity was evaluated by CV in 1.0 M KOH + 0.1 M $NH_3$ solution under the same rotating speed. CA experiments were conducted to evaluate the stability of electrocatalysts by maintaining a constant potential of 0.65 V versus RHE.

**In situ Raman characterizations.** In situ Raman experiments were conducted on a Raman spectrometer (HR evolution, Horiba Jobin Yvon, France) with a 532 nm solid laser as an excitation source. The measurements were performed in a customized electrolytic cell with a conventional three-electrode system. The carbon paper (1 cm × 1 cm) loaded with 0.5 mg of catalysts served as the working electrode, while an Ag/AgCl electrode and a Pt wire electrode functioned as the reference and counter electrodes, respectively. The electrolyte for the reaction was a mixture of 1.0 M KOH and 0.1 M $NH_3$, and the Raman spectra were acquired with a recording interval of 10 min per position.

**DAFC fabrication**. To prepare anode catalytic layer, 9.0 mg as-prepared catalysts and 2.5 mg carbon black were added into the mixture containing 200 μL 5 wt.% Nafion solution and 5 mL ethanol. Then, the catalyst ink was sprayed onto the carbon paper gas diffusion layer to fabricate a 9 $cm^2$ electrode with a loading of 1.0 $mg_{Pt}$ $cm^{-2}$. Carbon

paper loaded with A-$Pt_xNi_y$@NPC or PtIr/C 40% was used as the anode, and carbon paper loaded with commercial Pt/C was used as the cathode. The alkaline polymer electrolyte membrane (Fumasep FAAM-15) was pre-treated by soaking in a 5.0 M KOH solution for 24 h and then used as the separator. A 7.0 M $NH_3$ + 1.25 M KOH solution was used as the electrolyte. Polarization curves were acquired on the freshly assembled cell using a CS150M electrochemical workstation at an operating temperature of 60 ℃.

**DFT computational method and model.** The A-Pt@NPC, A-$Pt_{10}Ni_1$@NPC, A-$Pt_7Ni_1$@NPC, and A-$Pt_5Ni_1$@NPC were built based on a bilayered Pt surface and monolayer nitrogen-doped graphene structure, where the vacuum space along the z direction is set to be 20 Å, which is enough to avoid interaction between the two neighboring configurations. During the modeling process, Ni atoms were introduced into the top and second layers of the Pt slab to substitute corresponding Pt atoms. Given the inherent randomness of atomic distribution in solid-solution alloys, multiple possible arrangements were screened for thermodynamic stability, and the configurations with the lowest total energy were selected for subsequent catalytic property evaluations. The first principles calculations in the framework of density functional theory were carried out using the VASP package. The exchange-correlation functional under the generalized gradient approximation (GGA) with norm-conserving pseudopotentials and Perdew-Burke-Ernzerhof functional were adopted to describe the electron-electron interaction. An energy cutoff of 520 eV was used and a k-point sampling set of 3 × 3 × 1 was tested to be converged. The criterion for all structural optimizations was set to $10^{-5}$ eV for electronic energy convergence and Hellmann-Feynman force less than 0.02 eV $Å^{-1}$ for ionic relaxation loop. The van der Waals interaction was treated by Grimme scheme (DFT-D3). The implicit solvent model, VASPsol, was applied to consider the effects between the solute and solvent on the activation energies.

Adsorption energy $\Delta E$ of intermediates A on the surface of substrates was defined as:

$$\Delta E_{ads} = E_{*A} - (E^* + E_A) \quad (2)$$

where *A and * denoted the adsorption of intermediates A on substrates and the bare substrates, $E_A$ denoted the energy of A ion.

Free energy change $\Delta G$ of the reaction was calculated as the difference between

the free energies of the initial and final states as shown below:

$$\Delta G = \Delta E_{ads} + \Delta ZPE - T\Delta S \quad (3)$$

where $\Delta ZPE$ is the change of zero point energy; $T$ = 298.15 K and $\Delta S$ denote temperature and change of entropy, respectively.

**Table S1.** Inductively coupled plasma optical emission spectrometry (ICP-OES) analysis of different samples.

| Samples | Pt wt.% | Ni wt.% |
|---|---|---|
| **A-$Pt_{10}Ni_1$@NPC** | 16.04 | 0.47 |
| **A-$Pt_7Ni_1$@NPC** | 15.50 | 0.68 |
| **A-$Pt_5Ni_1$@NPC** | 14.74 | 0.90 |

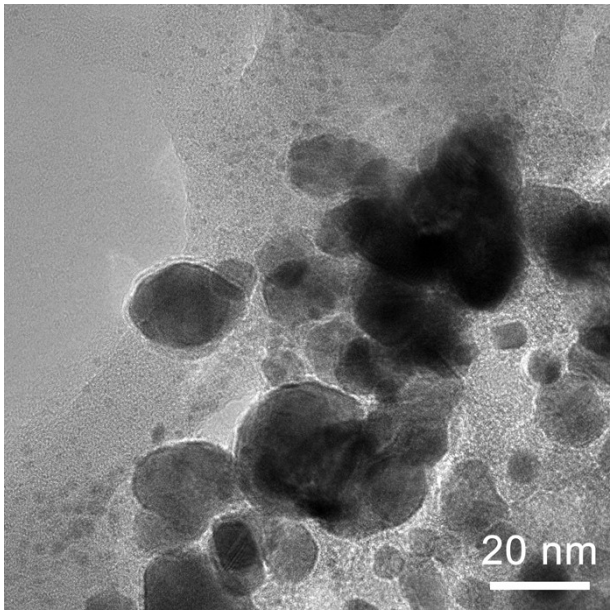


**Figure S1.** TEM image of A-$Pt_7Ni_1$@NPC.

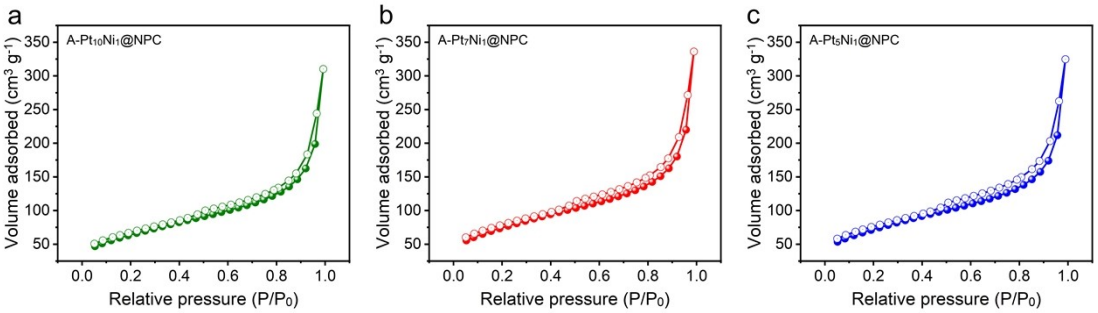


**Figure S2.** $N_2$ adsorption-desorption isotherms of (a) A-$Pt_{10}Ni_1$@NPC, (b) A-$Pt_7Ni_1$@NPC, and (c) A-$Pt_5Ni_1$@NPC.

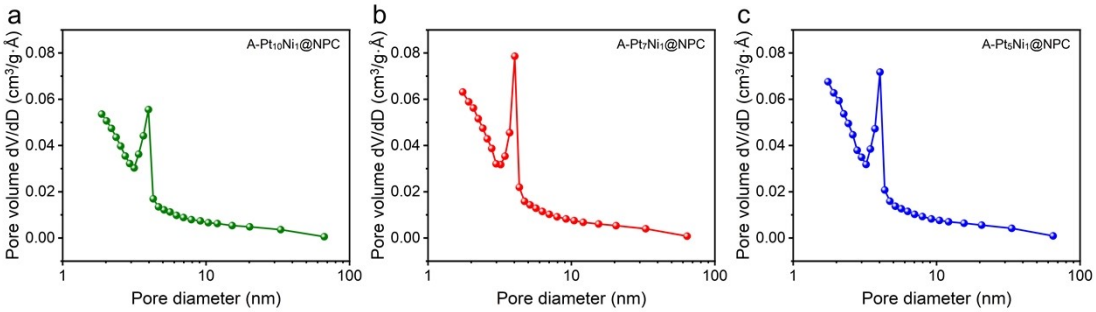


**Figure S3.** The pore size distributions of (a) A-$Pt_{10}Ni_1$@NPC, (b) A-$Pt_7Ni_1$@NPC, and (c) A-$Pt_5Ni_1$@NPC.

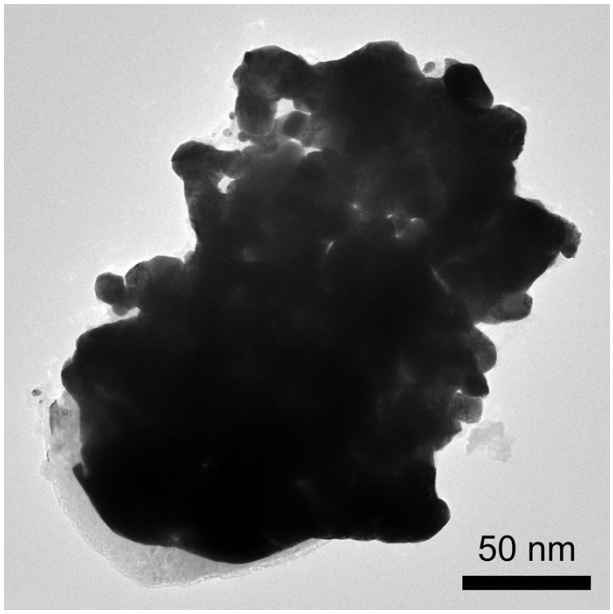


**Figure S4.** TEM image of the control synthesized under identical conditions but in the complete absence of sodium alginate.

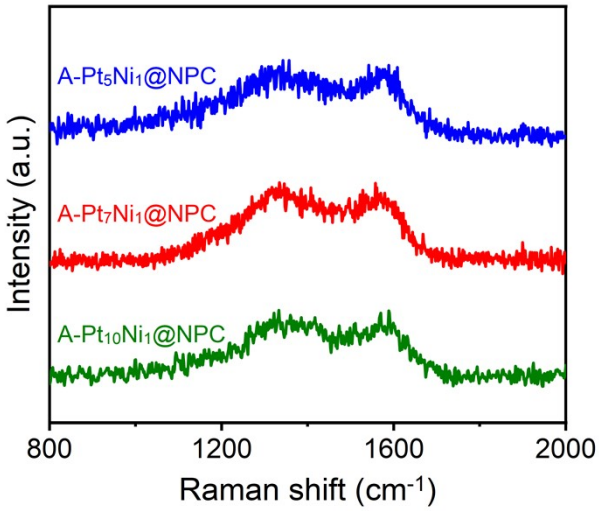


**Figure S5.** Raman patterns of different samples.

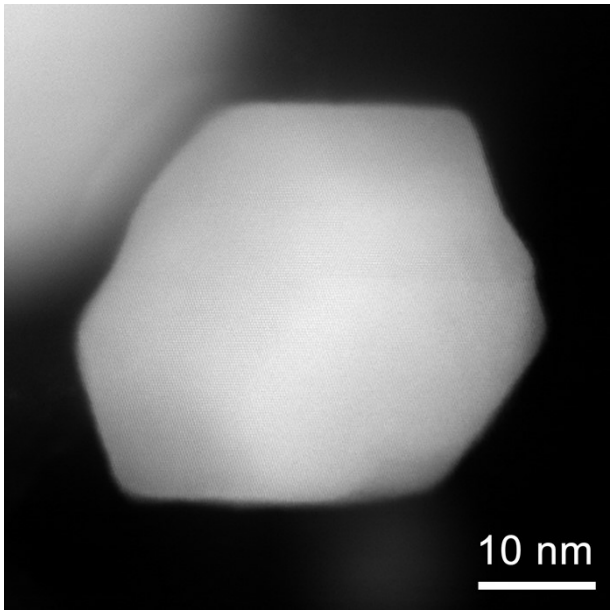


**Figure S6.** AC-HAADF-STEM image of A-$Pt_7Ni_1$@NPC.

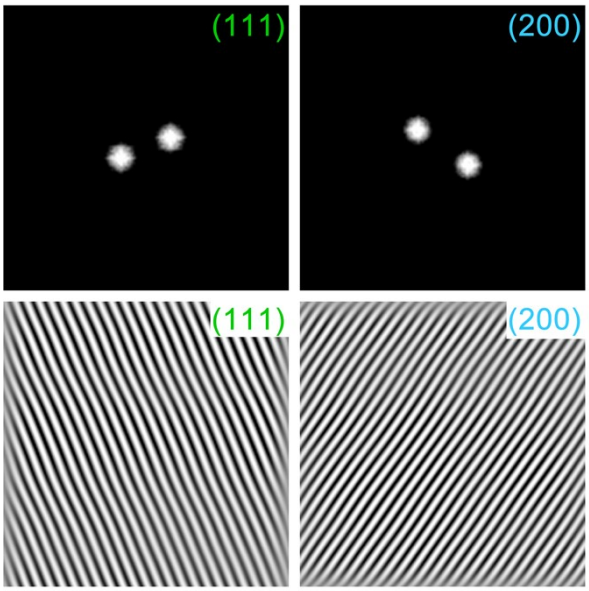


**Figure S7.** IFFT images of A-$Pt_7Ni_1$@NPC corresponding to diffraction spots of (111) and (200).

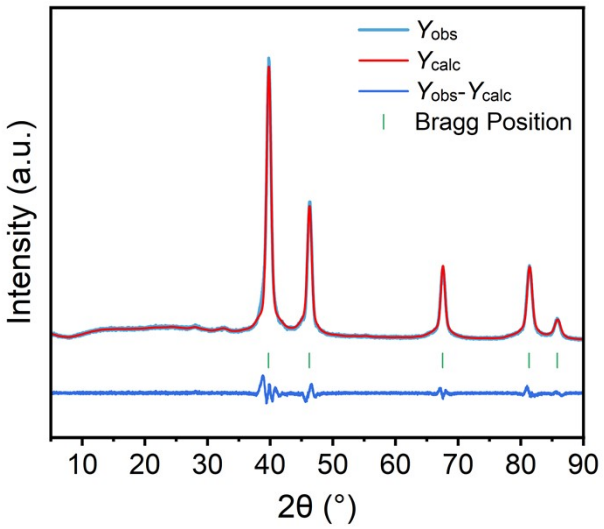


**Figure S8.** Rietveld refinement of the X-ray diffraction (XRD) pattern for the representative A-$Pt_7Ni_1$@NPC catalyst.

**Table S2.** Binding energies of high-resolution Pt 4f for different samples.

| Sample | Pt $4f_{5/2}$ (eV) | Pt $4f_{7/2}$ (eV) |
|---|---|---|
| **A-$Pt_5Ni_1$@NPC** | 73.95 | 70.60 |
| **A-$Pt_7Ni_1$@NPC** | 74.14 | 70.79 |
| **A-$Pt_{10}Ni_1$@NPC** | 74.24 | 70.89 |
| **Commercial Pt/C** | 74.91 | 71.56 |

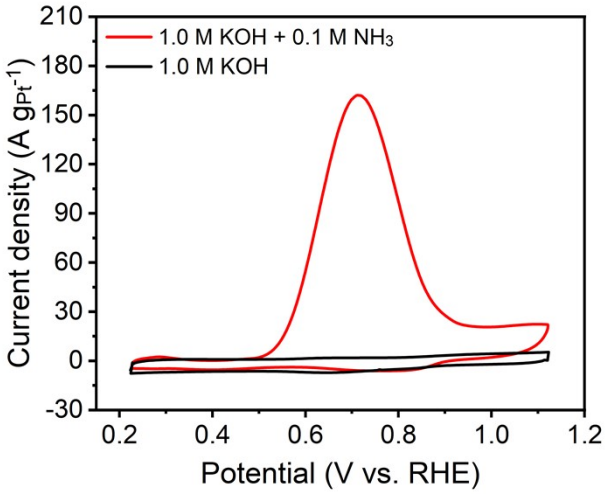


**Figure S9.** CV curves of A-$Pt_7Ni_1$@NPC in the presence and absence of $NH_3$ at a scan rate of 5 mV $s^{-1}$.

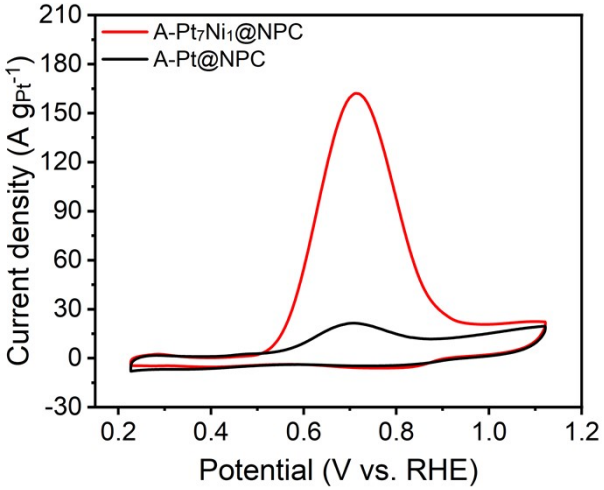


**Figure S10.** CV curves of A-$Pt_7Ni_1$@NPC and A-Pt@NPC in 1.0 M KOH + 0.1 M $NH_3$ at a scan rate of 5 mV $s^{-1}$.

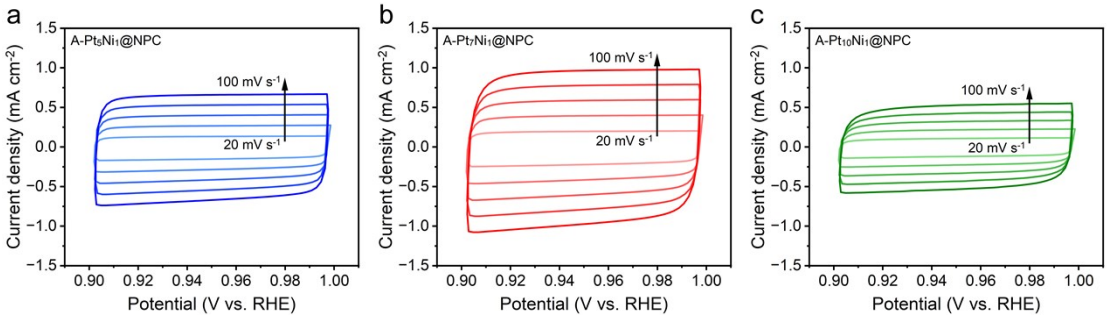


**Figure S11.** CV curves of (a) A-$Pt_5Ni_1$@NPC, (b) A-$Pt_7Ni_1$@NPC, and (c) A-$Pt_{10}Ni_1$@NPC measured at different scan rates from 20 to 100 mV $s^{-1}$.

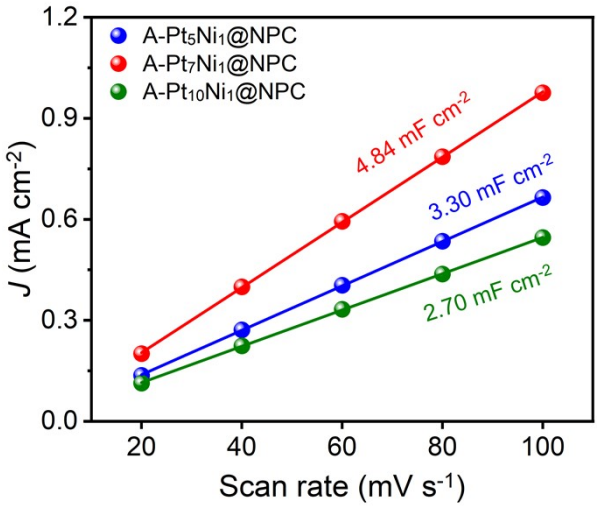


**Figure S12.** The $C_{dl}$ of A-$Pt_{10}Ni_1$@NPC, A-$Pt_7Ni_1$@NPC, and A-$Pt_5Ni_1$@NPC.

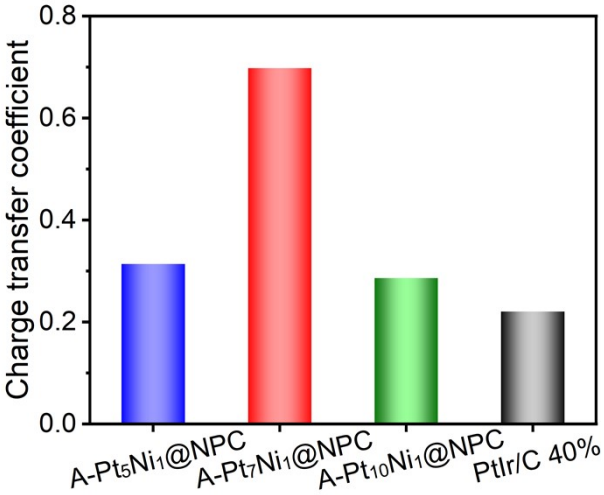


**Figure S13.** Charge transfer coefficients of different samples.

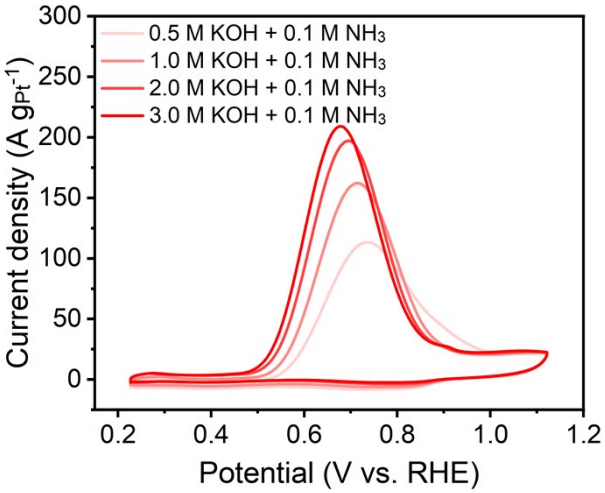


**Figure S14.** CV curves of the A-$Pt_7Ni_1$@NPC recorded in electrolytes containing 0.1 M $NH_3$ with varying KOH concentrations at a scan rate of 5 mV $s^{-1}$.

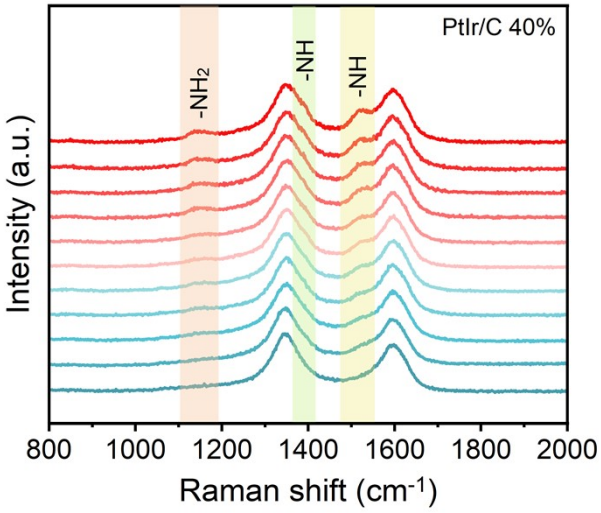


**Figure S15.** In situ Raman spectra of commercial PtIr/C 40% as a function of time.

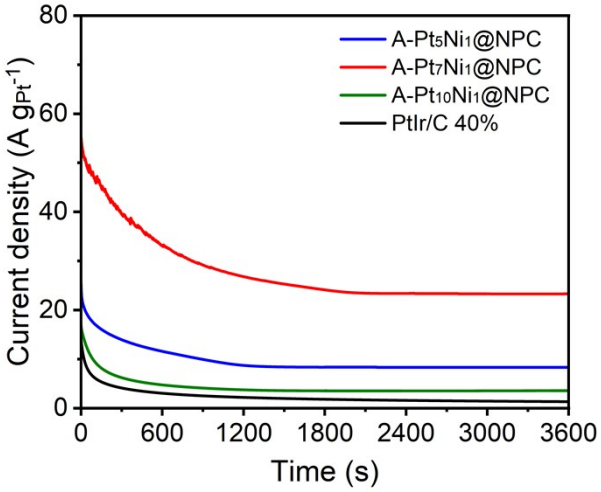


**Figure S16.** Chronoamperometric curves of different samples in 1.0 M KOH + 0.1 M $NH_3$ under ambient conditions.

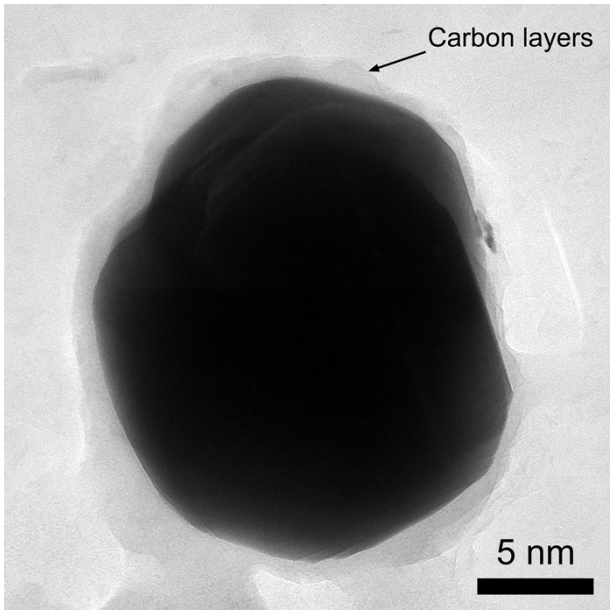


**Figure S17.** TEM image of the A-$Pt_7Ni_1$@NPC catalyst after the stability test.

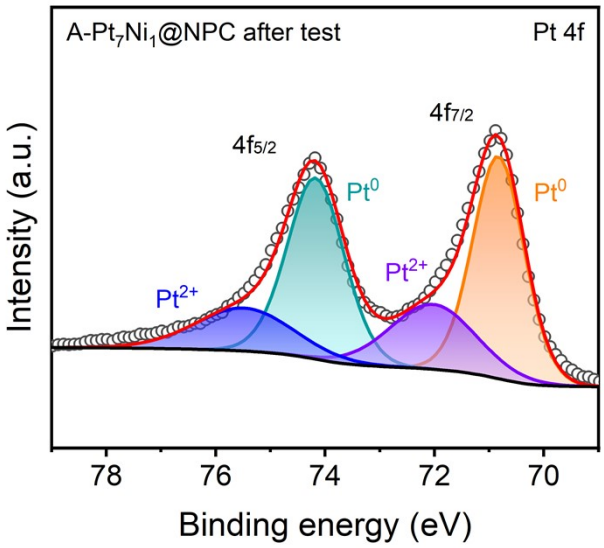


**Figure S18.** High-resolution Pt 4f XPS spectrum of the A-$Pt_7Ni_1$@NPC catalyst after the stability test.

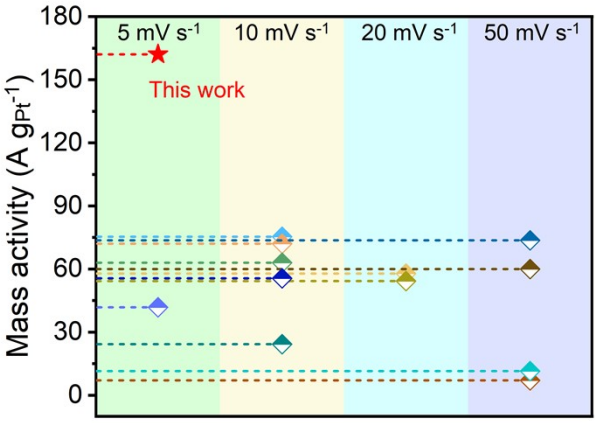


**Figure S19.** The comparison of mass activity of A-$Pt_7Ni_1$@NPC with the reported catalysts for the AOR.

**Table S3.** Comparison of the AOR performances with literature results.

| Catalyst | Electrolyte | Scan rate ($mV\ s^{-1}$) | Mass Activity ($A\ g_{Pt}^{-1}$)[#] | Ref. |
|---|---|---|---|---|
| **A-$Pt_7Ni_1$@NPC** | 1 M KOH + 0.1 M $NH_3$ | 5 | 162.07 | **This work** |
| **A-$Pt_5Ni_1$@NPC** | 1 M KOH + 0.1 M $NH_3$ | 5 | 34.52 | |
| **A-$Pt_{10}Ni_1$@NPC** | 1 M KOH + 0.1 M $NH_3$ | 5 | 20.81 | |
| **Pt nanoparticle** | 1 M KOH + 0.2 M $NH_4OH$ | 50 | 7.05 | [1] |
| **$Ni_{93}Pd_7$** | 0.5 M $NaNO_3$ + 200 mM $NH_4NO_3$ | 50 | 60.00 | [2] |
| **Pt-CNT 160 °C** | 1 M KOH + 1 M $NH_3$ | 10 | 24.27 | [3] |
| **Pt/Ir/MWCNT nanoparticle** | 0.1 M KOH + 0.1 M $NH_3$ | 50 | 11.50 | [4] |
| **Pt/$CeO_2$-ZIF-8** | 1 M KOH + 0.1 M $NH_3$ | 5 | 41.80 | [5] |
| **$SnO_2$-Pt/C** | 1 M KOH + 0.1 M $NH_3$ | 20 | 54.29 | [6] |
| **C-Pt/$SnO_2$** | 1 M KOH + 0.1 M $NH_3$ | 20 | 57.86 | |
| **Flower-like Pt** | 1 M KOH + 0.1 M $NH_3$ | 10 | 63.00 | [7] |
| **Coral-like Pt nanowires** | 1 M KOH + 0.05 M $(NH_4)_2SO_4$ | 10 | 72.00 | [8] |
| **Pt modified Ni particles** | 1 M KOH + 0.1 M $NH_3$ | 10 | 75.32 | [9] |
| **Pt/NG (1–1)** | 1 M KOH + 0.1 M $NH_3$ | 10 | 55.60 | [10] |

[#]The mass activities of all catalysts listed in this table are uniformly normalized based solely on the specific mass of Pt.

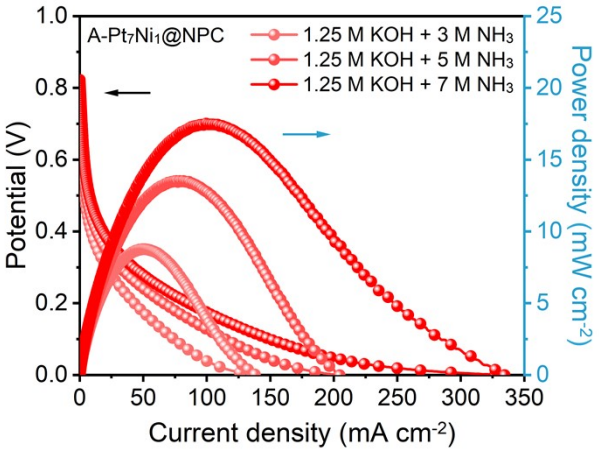


**Figure S20.** Polarization and power density curves of the assembled DAFC employing the A-$Pt_7Ni_1$@NPC anode under varying $NH_3$ feed concentrations.

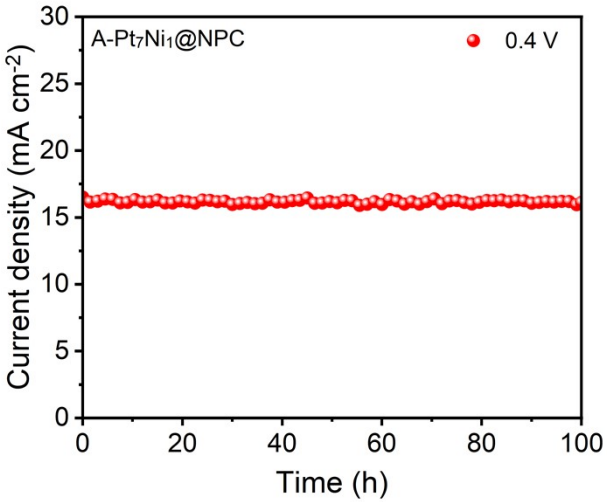


**Figure S21.** I-t curve of the A-$Pt_7Ni_1$@NPC-based DAFC recorded at 0.4 V for 100 h.

**Table S4.** Comparison of low-temperature DAFC performances with literature results.

| Anode | Cathode | Fuel | Operating temperature (°C) | Peak power density (mW $cm^{-2}$) | Ref. |
|---|---|---|---|---|---|
| **A-$Pt_7Ni_1$@NPC** | Pt/C | 1.25 M KOH + 7 M $NH_3$ | 60 | 17.51 | **This work** |
| **A-$Pt_5Ni_1$@NPC** | Pt/C | 1.25 M KOH + 7 M $NH_3$ | 60 | 11.76 | |
| **A-$Pt_{10}Ni_1$@NPC** | Pt/C | 1.25 M KOH + 7 M $NH_3$ | 60 | 7.36 | |
| **PtIr/C** | Pt/C | $NH_3$-Air | 25 | 1.68 | [11] |
| **PdIr/C** | Pt/C | 1 M KOH + 5 M $NH_4OH$ | 50 | 3.71 | [12] |
| **NiCu/C** | $SrCo_{0.8}Cu_{0.1}Nb_{0.1}O_{3-\delta}$/C | 1 M KOH + 35 wt.% $NH_3$ | 25 | 0.25 | [13] |
| **$Pt_7Co_2$-N-C** | $Pt_7Co_2$-N-C | 7 M $NH_3$ + 1.25 M KOH | 60 | 11.83 | [14] |
| | Pt/C | 7 M $NH_3$ + 1.25 M KOH | | 5.97 | |
| **Pt/C** | Pt/C | 25 wt.% $NH_4OH$ | 80 | 0.22 | [15] |
| **PtIr/C** | Pt/C | 1 M KOH + 5 M $NH_4OH$ | 40 | 4.17 | [16] |
| **IrRh/C** | Pt/C | 1 M KOH + 2 M $NH_4OH$ | 50 | 2.75 | [17] |
| **Pt/C** | Pt/C | $NH_3$ gas | 25 | 6.40 | [18] |
| **PtAu/C** | Pt/C | 1 M KOH + 5 M $NH_4OH$ | 40 | 2.64 | [19] |
| **$Y_2O_3$-modified Pt/C** | Pt/C | AEM | 50 | 6.33 | [20] |
| **PtCo-60** | 20 wt.% Pt/C | 3 M KOH + 3 M $NH_4OH$ | 80 | 11.33 | [21] |
| **PtRu/C** | Pt/C | $NH_3$ gas | 50 | 3.07 | [22] |

**Table S5.** Calculated Gibbs free energies of the reaction intermediates for the AOR on various catalysts.

| Configurations | Reaction coordinate | Gibbs free energy (eV) |
|---|---|---|
| **A-Pt@NPC** | $NH_3$ | 0 |
| | $*NH_3$ | -0.959 |
| | $*NH_2$ | 0.093 |
| | $*N_2H_4$ | 1.350 |
| | $*N_2H_3$ | 0.507 |
| | $*N_2H_2$ | 1.086 |
| | $*N_2H$ | 0.639 |
| | $*N_2$ | -0.400 |
| | $N_2$ | 0.340 |
| **A-$Pt_{10}Ni_1$@NPC** | $NH_3$ | 0 |
| | $*NH_3$ | -1.179 |
| | $*NH_2$ | -0.319 |
| | $*N_2H_4$ | 0.756 |
| | $*N_2H_3$ | 1.030 |
| | $*N_2H_2$ | 1.011 |
| | $*N_2H$ | -0.390 |
| | $*N_2$ | 0.371 |
| | $N_2$ | 0.340 |
| **A-$Pt_7Ni_1$@NPC** | $NH_3$ | 0 |
| | $*NH_3$ | -1.518 |
| | $*NH_2$ | -1.134 |
| | $*N_2H_4$ | -0.423 |
| | $*N_2H_3$ | 0.251 |
| | $*N_2H_2$ | 0.492 |
| | $*N_2H$ | -0.841 |
| | $*N_2$ | -0.168 |
| | $N_2$ | 0.340 |
| **A-$Pt_5Ni_1$@NPC** | $NH_3$ | 0 |
| | $*NH_3$ | -1.263 |
| | $*NH_2$ | -0.409 |
| | $*N_2H_4$ | 0.464 |
| | $*N_2H_3$ | -0.288 |
| | $*N_2H_2$ | 0.143 |
| | $*N_2H$ | 0.151 |
| | $*N_2$ | -0.295 |
| | $N_2$ | 0.340 |

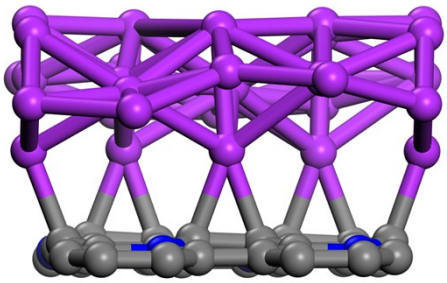

**Figure S22.** Atomic structural model of A-Pt@NPC.

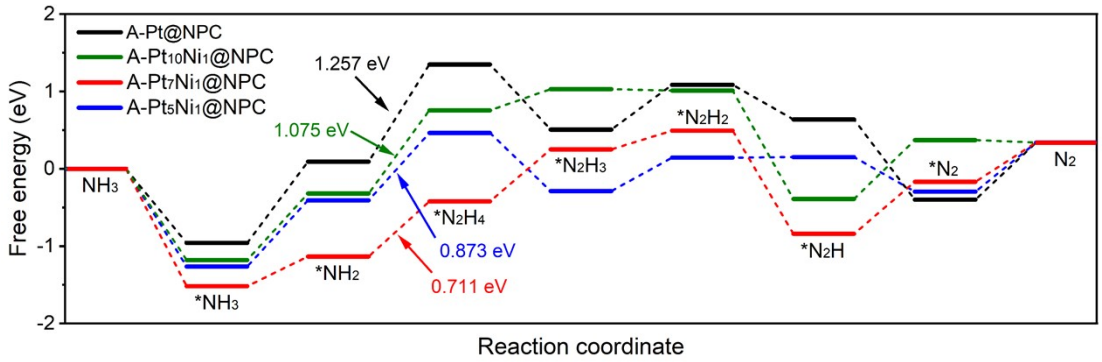


**Figure S23.** Gibbs free energy diagrams for the AOR on different catalyst models.

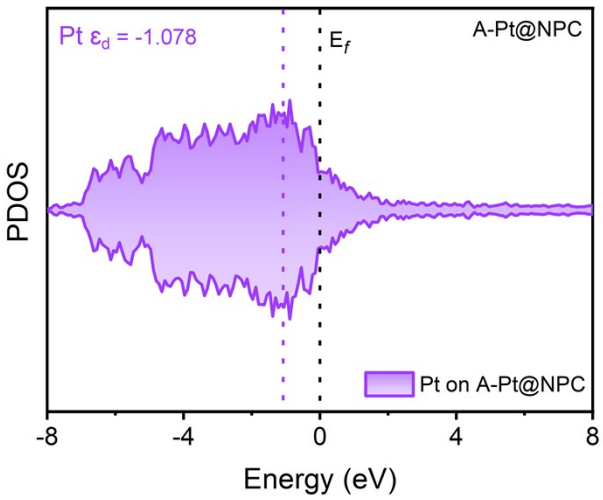


**Figure S24.** PDOS of Pt 5d orbital in A-Pt@NPC.

## References


[1] S. Ntais, A. Serov, N. I. Andersen, A. J. Roy, E. Cossar, A. Allagui, Z. Lu, X. Cui, E. A. Baranova, P. Atanassov, *Electrochim. Acta* **2016**, *222*, 1455-1463.

[2] A. Allagui, S. Sarfraz, E. A. Baranova, *Electrochim. Acta* **2013**, *110*, 253-259.

[3] N. Hanada, Y. Kohase, K. Hori, H. Sugime, S. Noda, *Electrochim. Acta* **2020**, *341*, 136027.

[4] S. Morita, E. Kudo, R. Shirasaka, M. Yonekawa, K. Nagai, H. Ota, M. N.-Gamo, H. Shiroishi, *J. Electroanal. Chem.* **2016**, *762*, 29-36.

[5] Y. Li, H. S. Pillai, T. Wang, S. Hwang, Y. Zhao, Z. Qiao, Q. Mu, S. Karakalos, M. Chen, J. Yang, D. Su, H. Xin, Y. Yan, G. Wu, *Energy Environ. Sci.* **2021**, *14*, 1449-1460.

[6] T. Okanishi, Y. Katayama, H. Muroyama, T. Matsui, K. Eguchi, *Electrochim. Acta* **2015**, *173*, 364-369.

[7] J. Liu, C. Zhong, Y. Yang, Y. T. Wu, A. K. Jiang, Y. D. Deng, Z. Zhang, W. B. Hu, *Int. J. Hydrogen Energy* **2012**, *37*, 8981-8987.

[8] J. Liu, Z. Liu, H. Wang, B. Liu, N. Zhao, C. Zhong, W. Hu, *Adv. Funct. Mater.* **2021**, *32*, 2110702.

[9] J. Liu, B. Chen, Y. Kou, Z. Liu, X. Chen, Y. Li, Y. Deng, X. Han, W. Hu, C. Zhong, *J. Mater. Chem. A* **2016**, *4*, 11060-11068.

[10] Y. Zhou, G. Zhang, Z. Gong, X. Shang, F. Yang, *ChemElectroChem* **2016**, *3*, 605-614.

[11] R. Chen, S. Zheng, Y. Yao, Z. Lin, W. Ouyang, L. Zhuo, Z. Wang, *Int. J. Hydrogen Energy* **2021**, *46*, 27749-27757.

[12] M. H. M. T. Assumpção, S. G. da Silva, R. F. B. De Souza, G. S. Buzzo, E. V. Spinacé, M. C. Santos, A. O. Neto, J. C. M. Silva, *J. Power Sources* **2014**, *268*, 129-136.

[13] P. Zou, S. Chen, R. Lan, S. Tao, *ChemSusChem* **2019**, *12*, 2788-2794.

[14] F. Fang, Q. Cheng, M. Wang, Y. He, Y. Huan, S. Liu, T. Qian, C. Yan, J. Lu, *ACS Nano* **2025**, *19*, 1260-1270.

[15] K. R. Lee, D. Song, S. B. Park, J.-i. Han, *RSC Adv.* **2014**, *4*, 5638-5641.

[16] M. H. M. T. Assumpção, S. G. da Silva, R. F. B. de Souza, G. S. Buzzo, E. V. Spinacé, A. O. Neto, J. C. M. Silva, *Int. J. Hydrogen Energy* **2014**, *39*, 5148-5152.

[17] J. C. M. Silva, M. H. M. T. Assumpção, P. Hammer, A. O. Neto, E. V. Spinacé, E. A. Baranova, *ChemElectroChem* **2017**, *4*, 1101-1107.

[18] O. Siddiqui, I. Dincer, *Fuel Cells* **2018**, *18*, 379-388.

[19] J. C. M. Silva, S. G. da Silva, R. F. B. De Souza, G. S. Buzzo, E. V. Spinacé, A. O. Neto, M. H. M. T. Assumpção, *Appl. Catal. A* **2015**, *490*, 133-138.

[20] Y. Katayama, T. Okanishi, H. Muroyama, T. Matsui, K. Eguchi, *J. Catal.* **2016**, *344*, 496-506.

[21] C.-E. Hong, D.-H. Park, Y. Gu, S.-H. Park, D.-M. Lim, D.-G. Seo, J.-I. Han, K.-W. Park, *Int. J. Hydrogen Energy* **2024**, *87*, 1367-1376.

[22] S. Suzuki, H. Muroyama, T. Matsui, K. Eguchi, *J. Power Sources* **2012**, *208*, 257-262.